Article

A Numerical Study of Sub-Millisecond Integrated Mix-and-Inject Microfluidic Devices for Sample Delivery at Synchrotron and XFELs

Majid Hejazian *[ID], **Eugeniu Balaur** [ID] **and Brian Abbey**

ARC Centre of Excellence in Advanced Molecular Imaging, Department of Chemistry and Physics, La Trobe Institute for Molecular Sciences, La Trobe University, Bundoora, VIC 3086, Australia; e.balaur@latrobe.edu.au (E.B.); b.abbey@latrobe.edu.au (B.A.)
* Correspondence: m.hejazian@latrobe.edu.au

Abstract: Microfluidic devices which integrate both rapid mixing and liquid jetting for sample delivery are an emerging solution for studying molecular dynamics via X-ray diffraction. Here we use finite element modelling to investigate the efficiency and time-resolution achievable using microfluidic mixers within the parameter range required for producing stable liquid jets. Three-dimensional simulations, validated by experimental data, are used to determine the velocity and concentration distribution within these devices. The results show that by adopting a serpentine geometry, it is possible to induce chaotic mixing, which effectively reduces the time required to achieve a homogeneous mixture for sample delivery. Further, we investigate the effect of flow rate and the mixer microchannel size on the mixing efficiency and minimum time required for complete mixing of the two solutions whilst maintaining a stable jet. In general, we find that the smaller the cross-sectional area of the mixer microchannel, the shorter the time needed to achieve homogeneous mixing for a given flow rate. The results of these simulations will form the basis for optimised designs enabling the study of molecular dynamics occurring on millisecond timescales using integrated mix-and-inject microfluidic devices.

Keywords: microfluidics; micro-jet; sub-millisecond mixing; simulation; sample delivery for X-ray free-electron laser (XFEL)

1. Introduction

The availability of synchrotron and X-ray free-electron laser (XFEL) radiation sources enables time-resolved studies of structural changes in biomolecules to be carried out with atomic resolution [1]. A key challenge with performing these types of experiments is how to efficiently deliver molecules to the X-ray beam and then rapidly trigger dynamic changes on the relevant molecular timescales. In order to address the first problem, devices capable of forming liquid micro-jets have been developed which offer precise control over the size of the interaction region and produce minimal background signal [2–6]. For the second problem of triggering a reaction, microfluidics offers a number of advantages in terms of efficiently and homogeneously mixing reactants such that the subsequent molecular dynamics can be probed by illuminating different points on the liquid jet with the X-ray beam. Benefits of using microfluidic devices for studying molecular dynamics include the ability to combine multiple fluidic components on a single chip, the flexibility of the geometries that can be produced, and the reproducibility in terms of fabrication. The use of microfluidics also enables a high surface-to-volume ratio to be used, enhancing heat and mass transfer whilst ensuring a low Reynolds number, i.e., the laminar flow regime. In this scenario, the viscous forces dominate over the inertial forces within the flow, which dampens any flow irregularities that might occur in the fluid [7]. However, in the laminar flow regime, there is a requirement for comparatively long mixing channels, as mixing

predominantly occurs via low-efficiency diffusion, which limits the temporal resolution than can be achieved using diffusion-based micromixers.

A promising method to overcome the limitations imposed by mixing in straight microchannels is to employ passive mixing techniques, which are able to enhance mixing by inducing chaotic behaviours that are not present in linear channels [7,8]. A typical approach to enhanced passive mixing is exploiting unusual geometries in the mixing channels to achieve a chaotic advection effect. The chaotic effect increases the effective contact surface area and overall contact time between the reactants, which results in an improved mixing efficiency compared to just a straight microchannel [9]. Examples of enhanced passive mixing strategies employed in micromixers include the use of intersecting channels [10–15], the addition of curvatures [16–18], and the inclusion of obstacles or barriers to the liquid flow [19–23]. For example, Solehati et al. [24] conducted a numerical study comparing the mixing efficiencies of wavy and straight T-junction micromixers. They reported higher mixing efficiencies for the wavy micromixer because a chaotic flow regime could be induced. This is consistent with the fact that the chaotic advection effect increases at higher Reynolds numbers, making wavy micromixers more efficient at higher flow rates. In a related study, Chen et al. [25] carried out a series of COMSOL [26] finite element method (FEM) simulations comparing the efficiency of standard zig-zag micromixers to a topologically optimised zig-zag micromixer, including additional obstacles. Their results show that additional blocks to the liquid flow create more secondary flow and chaotic effects within the mixer, resulting in higher efficiencies. However, the use of obstacles negatively impacts the width of the microchannels, which can result in a higher rate of blockage within the device. For example, working with micro-crystals or even biomolecules means that there is often debris or organic material within the liquid flow, which can become trapped against any barriers or obstacles which may exist.

Passive mixing using microfluidics has been widely implemented in order to investigate the kinetics of biochemical reactions owing to the fast (milli- and microsecond) mixing times achievable, comparatively low sample consumption rates, and ease of integration with different experimental setups [27]. Employing droplet microfluidics in combination with passive micro-mixing further decreases sample consumption whilst allowing for a wide range of possible mixing times. For example, Jiang et al. [28] used two-photon fluorescence lifetime imaging microscopy combined with FEM simulations (using COMSOL) to generate 2D maps of chaotic mixing patterns inside of microdroplets travelling through a serpentine mixer. Their experimental and simulation results showed that their micro-mixer could achieve mixing efficiencies of up to 80% after just 18 ms. Of particular relevance to the current work is the fact that by forcing the droplets through sharp turns within a serpentine mixing channel, the authors were able to demonstrate the introduction of chaotic mixing within the droplets, which in turn enhanced the mixing efficiency. Another study of chaotic mixing in serpentine channels was carried out by Song and Ismagilov [29], who examined the millisecond kinetics of an enzymatic reaction by measuring the fluorescence intensities using nanolitre droplets. Micromixers have also been used for crystallisation studies; for example, Chen et al. [30] utilised a passive micromixer consisting of multiple 3D crossing channels in order to optimise the production of silver azide (SA) crystals. In addition to achieving high mixing efficiencies and low reagent consumption, the micromixer allowed for the optimisation of the size and shape of crystals which was not possible using macroscale crystallisation approaches.

By employing micromixers, researchers have the means to trigger dynamic changes in proteins either in solution or as nanocrystals on sub-millisecond time scales. These timescales are suitable for studying large-scale conformal changes in proteins, such as folding and unfolding [31], which can be probed using a range of laboratory and synchrotron-based techniques including small-angle and wide-angle X-ray scattering (SAXS/WAXS). An example of a system that could benefit from the availability of sub-millisecond sample mixing and delivery is human ubiquitin, a key protein found in almost all human cellular tissue, whose conformational dynamics are still not well understood [32]. The

structural dynamics of the four-helix bundle within the FF Domain (where FF indicates the presence of two phenylalanines), which is found in a large number of nuclear proteins, from Human HYPA/FBP11 is also a suitable target. This has previously been studied using Nuclear Magnetic Resonance (NMR) spectroscopy [33]. A particularly promising avenue for studying molecular dynamics at the atomic scale is via either serial femtosecond nanocrystallography (SFX) [34] or SAXS/WAXS. Liu et al. and Kang et al. [35] previously used conventional capillary injectors to deliver protein solution to the X-ray beam in the form of a micro-jet for time-resolved SFX studies of G protein-coupled protein receptors.

In order to investigate the dynamics of proteins, a reaction must be initiated prior to measurement. To achieve the necessary sub-millisecond time-resolution, rapid, homogeneous mixing of the reactants is required immediately prior to measurement. Microfluidic devices incorporating micromixers and injector nozzles into one integrated structure (i.e., mix-and-inject) serve as the ideal platform for initiating and measuring molecular dynamics for time-resolved structural biology. Recently, Knoska et al. [36] have reported the development of an ultra-compact 3D microfluidic mix-and-inject device for performing time-resolved serial femtosecond crystallography (SFX) measurements. For their device, they used a two-photon additive manufacturing technique to produce an integrated 3D helical mixer. Kim et al. [37] have also previously produced a 3D serpentine micro-mixer in order to examine the dynamics of carbamates. The serpentine geometry they employed was again found to significantly enhance the mixing efficiency, enabling them to achieve a high synthesis throughput of 5.3 g/h with continuous flow. Maeots et al. [38] also used the same mixer design incorporating a nozzle for mixing-and-spraying a protein solution onto a copper grid for electron microscopy measurements. Using this approach, they were able to capture different conformations of RecA-ssDNA filaments using cryo-electron microscopy. Their mixer was able to achieve high mixing efficiencies (up to 90%) on millisecond mixing time scales (2–5 ms) using nanolitre volumes of the sample.

Although this work is the first simulation study examining chaotic mixing in integrated mix-and-inject devices, these types of effects in isolated micromixers have been reported on previously [17,19–22]. For example, Jones et al. [39] have carried out a parametric study of advection in order to investigate phenomena such as the stretching of interfaces and the chaotic stirring that occurs in micromixers incorporating twisted pipes. They reported that passive mixing utilising the chaotic effect enhances the mixing efficiency (stirring quality) which can be obtained without the need for adding any additional energy into the system. Whilst the influence of passive mixing on micromixers in isolation has been reported before in the literature, here, we are interested in investigating the range of parameters and mixing times that can be achieved using integrated mix-and-inject devices. Understanding and optimising these characteristics is critical to achieving the maximum time-resolution for molecular dynamics experiments. Such devices are currently used on both synchrotron and XFEL sources to study dynamic changes in proteins, and also have the potential to be deployed in a range of different molecular sensing applications. The two key aims with the present work are (1) to determine the influence of the device geometry on mixing performance under conditions of stable jetting and (2) to predict the minimum time required for homogeneous mixing, which will determine the limit on the timescales for the dynamic processes which can be studied.

Previously, we experimentally demonstrated the application of a new approach to fabricating planer microfluidic mix-and-inject devices based on high-resolution photolithography using SU8 on glass [40,41]. These devices have the advantage of being relatively straightforward to fabricate whilst having very high mechanical rigidity and chemical inertness. One of the primary applications for these devices is the investigation of molecular dynamics using X-ray diffraction at XFEL sources. In our previous experimental work, we used fluorescence intensity analysis to demonstrate millisecond and sub-millisecond combined mixing and jetting. To date, the new field of integrated mix-and-inject microfluidic devices has received much less attention in terms of numerical simulation studies than standalone micromixers. Integrated devices enable both rapid mixing and the stable

formation of a free-standing liquid microfluidic jet for sample delivery, which facilitates time-resolved molecular imaging studies. Here, we present micromixer simulations that are specifically conducted under conditions that are consistent with the formation of a stable jet. We determine the characteristics of these devices through numerical simulation to predict the minimum mixing time, using (partially) chaotic mixing, which is achieved with a serpentine micromixer. Characterising the mixing performance of these devices is an essential element in sample delivery in the context of imaging molecular dynamics at synchrotrons and XFELs. We also attempt to provide a guide for the optimisation of the mixing component for future molecular imaging studies to further reduce the mixing time whilst still maintaining stable liquid jet delivery. In the current simulation study, we employ an FEM analysis conducted using COMSOL in order to investigate the mixing behaviour, efficiency, and minimum achievable mixing times possible using these mix-and-inject devices for a wide range of different flow rates. The simulation results presented here are validated against the experimental data. We anticipate that this work will guide the development of future integrated mix-and-inject devices as well as help researchers to plan and design experiments aiming to capture sub-millisecond molecular dynamics.

2. Materials and Methods

2.1. Experimental Work

We have previously reported microfluidic mix-and-inject devices, which were optimised for molecular imaging studies at the European XFEL [40,41]. The microfluidic mix-and-inject devices were fabricated using a novel SU8-on-glass method that has not been reported previously. The efficiency of the serpentine micro-mixer component was determined using the fluorescent intensity analysis technique. The devices were also tested for their jetting performance, and 3 distinct jetting regimes were identified and reported. In the present paper, the goal is to explore, using numerical simulation, the mixing characteristics and minimum achievable mixing time that is possible using our integrated mix-and-inject sample delivery platform. The devices investigated here consist of an integrated serpentine micro-mixer channel and a gas dynamic virtual nozzle (GDVN), fabricated using our recently developed SU8 on glass technique [40,41]. The nominal width (W) and height (H) of the serpentine microchannel is 25 μm and 45 μm, respectively. The mixing performance was experimentally characterised using fluorescence measurements at five different positions along the micromixer channel, starting at just after the inlets. During the experimental measurements, three different types of the liquid jet (cylindrical, ribbon, and planer) were observed; the schematic in Figure 1 is an approximate representation of the regime (in terms of flow rate and gas pressure) over which combined homogeneous mixing and stable jetting can be achieved using our devices.

For the simulation study, the mixing behaviour of the microfluidic devices was investigated over a range of conditions for which both homogeneous mixing and stable jetting was observed experimentally shown in Figure 1. One of the key goals of the simulations was the characterisation of the mixer in terms of the minimum time required to achieve homogeneous mixing as a function of the flow rate and length of the serpentine mixer. This, in turn, determines the maximum time-resolution possible using these devices.

2.2. Geometric Structure of Microfluidic Devices

In order to characterise our devices, we considered the mixing of two solutions. For solution #1, we chose a 6.64 mM solution, matching the concentration of the fluorescein sodium salt in DI-water that was measured experimentally using our devices. Solution #2 was taken to be pure water. The two solutions (solution #1 and solution #2) conjugate via a Y-shaped junction, followed by a serpentine-shaped mixer comprising 19 turns. Within the COMSOL Multiphysics simulation package, the laminar flow and the transport of diluted species modules were employed. We defined 12 probe cross-sectional surfaces at which the device characteristics were probed (see Figure 2). When comparing to the experimental

data, the simulated cross-sectional surfaces were averaged along the y-axis, resulting in line profiles which could be directly matched to the fluorescence measurements.
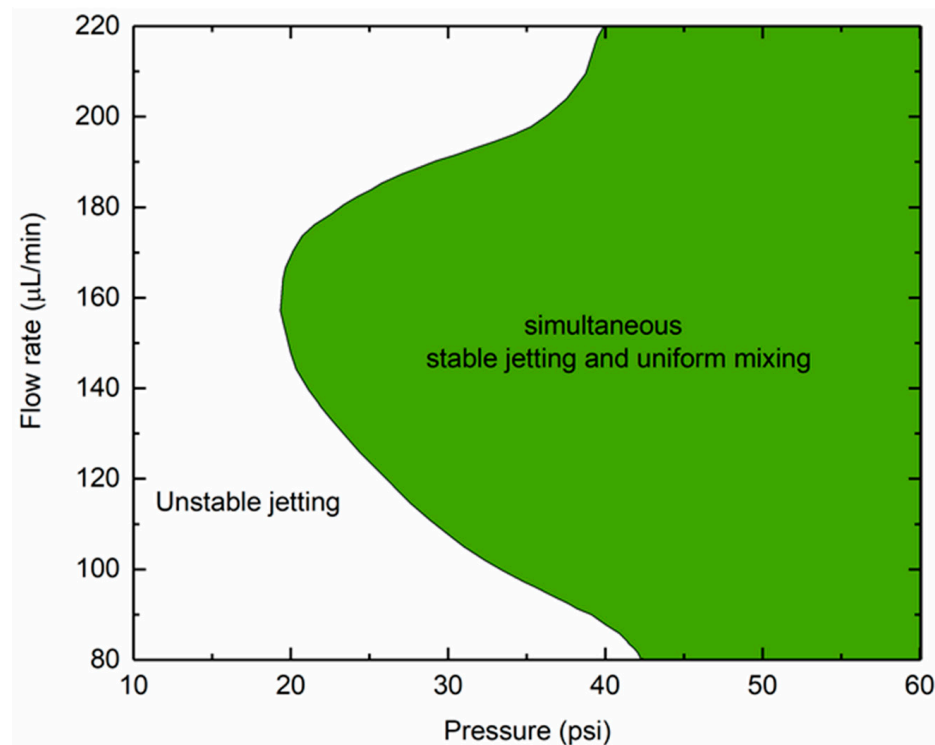
Figure 1. Schematic of the stable operating conditions for our mix-and inject microfluidic devices [40,41] based on optical experiments. Uniform mixing was observed to occur over a flow rate range of 80–220 μL/min. The green area indicates the optimal conditions where both uniform mixing and stable jetting were observed.
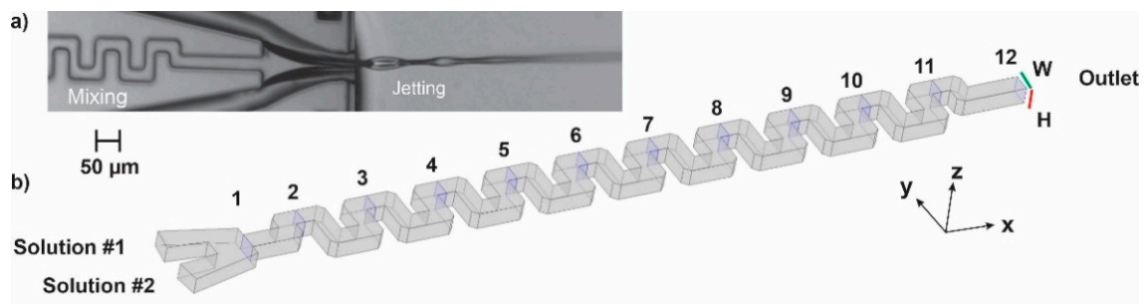
Figure 2. The mixing component of the microfluidic mix-and-inject device, (**a**) optical microscope image of the serpentine mixer fabricated using SU8 on glass; (**b**) schematic of the simulated geometry employed for the present study. The points at which the device characteristics (e.g., concentration) were probed are shown by the light blue squares in the cross-section of the mixer channel.

2.3. Governing Equations

For the simulations, we used a single-phase laminar fluid flow interface to model the diffusive/convective transport properties of the solutions in the mixer microchannel. All fluids were considered to be incompressible, and steady-state conditions were applied. The model solves the continuity equation:

$$\rho \nabla \cdot \mathbf{u} = 0 \tag{1}$$

and the Navier–Stokes equation,

$$\rho(\mathbf{u}\cdot\nabla)\mathbf{u} \;=\; \nabla\cdot[-p\mathbf{I} + \mathbf{K}] + \mathbf{F} \tag{2}$$

where ρ is the solution density (kg/m^3), u is the velocity vector (m/s), $\nabla()$ is the gradient operator, p is the pressure inside the mixer microchannel (Pa), **I** is the identity matrix, K is the viscous stress tensor (Pa), and F is the volume force vector (N/m^3). The diffusive/convective transport of a dilute solute is defined by:

$$-\nabla\cdot(-D\nabla c + c\mathbf{u}) \;=\; 0 \tag{3}$$

where c (mol/m^3) is the concentration, and D (m^2/s) is the diffusion coefficient of the solute. A diffusion coefficient of $D = 4.9 \times 10^{-10}$ m^2/s, consistent with the molecular diffusion of fluorescein in water, was used in the simulations [42]. The flow and mass transport models were used in order to solve the concentration distribution in the 3D domain.
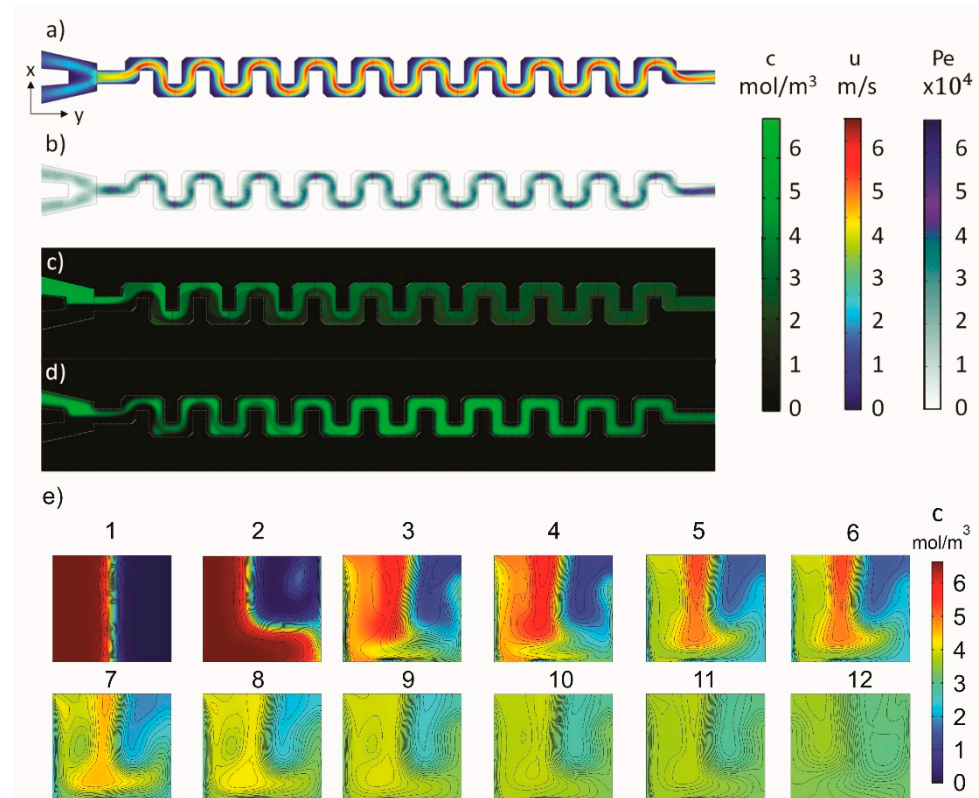
2.4. Numerical Simulations

At the walls of the micromixer, the no-slip condition was applied. The pressure, no viscous stress, boundary condition ($p = 0$), was assumed at the outlet, which specifies a vanishingly small viscous stress once the liquid flow encounters the external atmosphere. The flow rate was varied over a range of 80–220 µL/min, consistent with the stable jetting regime indicated in Figure 1. For the numerical solution of the governing equations, finite element discretisation based on linear functions for the velocity was used, whilst the pressure and concentration fields were described by second-order functions. A mesh consisting of 3,986,106 domain elements was used to represent the micromixer model. Figure 3 shows representative results for the flow field and concentration field at a flow rate of 80 µL/min.

Figure 3a shows the simulated velocity magnitude distribution within the serpentine micromixer. The serpentine geometry causes the maximum fluid velocity to vary, moving from the centre of the microchannel towards the edges along the *x*-direction [43]. This is a key characteristic required to induce chaotic flow in low Reynolds number microfluidic systems, where it is essential to have transverse components of liquid flow that stretch and fold volumes of fluid over the cross-section of the microfluidic channel. This is the mechanism via which the serpentine geometry induces stirring flows, which in turn leads to a decreased average distance over which the diffusion occurs. As the geometrical and liquid parameters are constant, the chaotic flow reaches a steady state, where the stretching and folding of volumes of the fluid proceed exponentially as a function of the axial distance travelled by the fluid volume. This is related to the characteristic length which depends on the geometry of the fabricated microfluidic system: $\Delta y = t \cdot exp(-\Delta x/l)$, where t is the initial transverse distance [44,45].

The Peclet number is a physical quantity defined as the ratio of the rate of the convective mass transport to the rate of diffusion mass transport. The Peclet number is given by $Pe = ul/D$, where l is the characteristic length (the distance over which the species must mix). In the present case where we have chaotic mixing occurring, the hydraulic diameter of the channel is defined as the characteristic length scale and is given by $4A/P_w$ where A is the cross-sectional area, and P_w is the wetted perimeter of the channel at the cross-section. For the present simulation, due to the low diffusivity of fluorescein in water and a relatively high-velocity range of 1.89–4.72 m/s, the maximum values of Pe are around 65,000. A large Pe indicates a convective dominated mass transport, which in this case is highly dependent on the chaotic advection phenomenon in the mixer microchannel [46]. The micro-mixer areas, where the chaotic advection effect is higher, are shown by the darker blue regions within the Peclet number distribution (Figure 3b). Figure 3b shows clear periodic perturbations, characteristic of the stretching and folding of fluid volumes, which are associated with chaotic advection. The darkest spots (highest Pe) in Figure 3b are in the centre of the U-bend shapes, indicating a constriction in the flow due to the resistance

created by the microchannel walls because of the serpentine geometry. The value of Pe also peaks near the outlet because of the sudden release of the flow due to the lack of microchannel wall resistance near the outlet.


Figure 3. Distribution plots in the x–y plane at a flow rate of 80 μL/min for (**a**) velocity, (**b**) Peclet number, and (**c**) concentration. The intensity of the Peclet number (Pe) distribution in (**b**) directly corresponds to the intensity of the chaotic advection effect (chaotic mixing is higher in darker areas). The chaotic mixing of the two solutions is also apparent from the concentration distribution shown in (**c**). (**d**) An experimental optical fluorescence image of mixing in the serpentine, also at 80 μL/min, shows the same chaotic effect as was observed in the serpentine microchannel during simulations. Note that the outline of the channel is indicated by the dotted white line in (**c**,**d**). (**e**) shows the cross-sectional concentration distributions and iso-concentration contours as a function of distance travelled along the serpentine (at the 12 probe points which are indicated in Figure 2).

The simulated concentration profile is shown in Figure 3c; this agrees well with the corresponding experimental optical fluorescence data, an example of which is shown in Figure 3d, providing additional confirmation of the accuracy and interpretation of our FEM model. In both simulated and experimental concentration profiles, there are light and dark bands visible along the serpentine channel due to the effects of chaotic advection. However, we note that there are some variations between the simulated and experimental data which we attribute to several factors. These include the fact that out-of-plane, the optical concentration profile data are measured within a narrow, but finite, region within the channel defined by the depth-of-focus of the microscope, whereas the simulated concentration profile is precisely defined at the mid-height (with respect to the z-axis) of the microfluidic channel. Another point to consider is that any errors in the fabrication, though confined to the (sub-) micron scale, may have an effect and this will also impact the concentration profile.

In order to further investigate the mixing characteristics, the slice concentration distributions and the cross-section iso-concentration contours for 12 probe positions at a flow rate of 80 μL/min are shown in Figure 3e. The velocity shift towards the centre affects

the concentration profile by disrupting the interface between solution #1 and solution #2, which otherwise would be dominated by diffusion.

Example concentration profiles for six probes along the serpentine micromixer at a flow rate of 80 μL/min are plotted in Figure 4. The solutions being mixed can be distinguished by the sharp concentration gradient between them near the Y-junction. At probe point #3, the effect of the chaotic flow in the microchannel results in an asymmetrical concentration distribution across the y-axis. As the solution progresses towards the outlet, the concentration profiles become more even and flat as the gradient across the y-axis decreases, indicating homogeneous mixing. At the outlet (probe point #12), the concentration gradient is close to zero, indicating that complete mixing has been achieved.
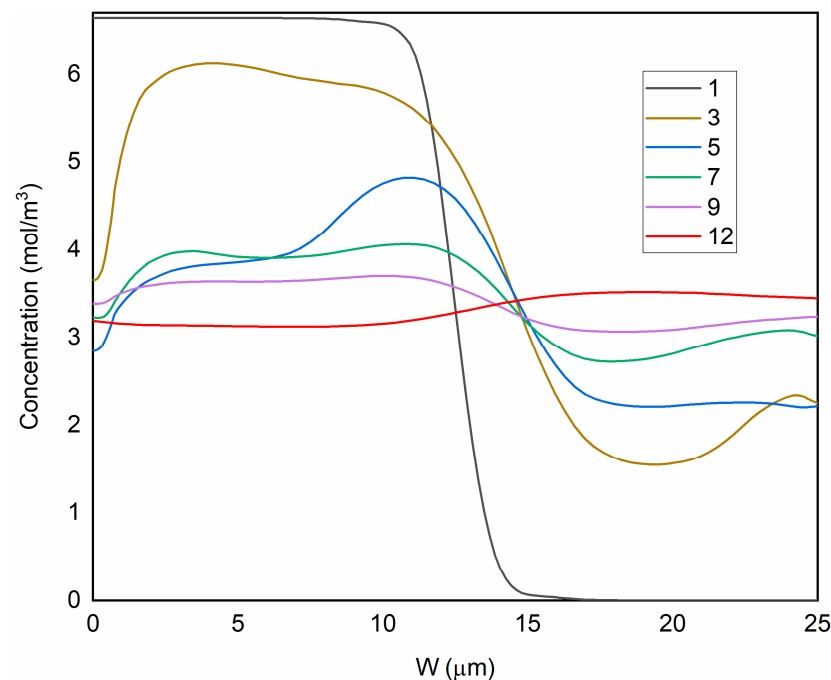
Figure 4. Concentration profiles at six positions (probe points #1, 3, 5, 7, 9, 12) across the width of the serpentine micromixer. The concentration curve at the inlet (#1, black) shows two distinct solutions with a sharp concentration gradient at the interface. The concentration curves flatten approaching the outlet and are almost completely flat near to the outlet point of the liquid jet (#12, red) indicating enhanced mixing induced by the chaotic advection effect of the serpentine geometry.

3. Results

3.1. Mixing Analysis

The degree of homogeneity of the concentration profile in any given cross-section of the mixer microchannel is a measure of the full mixing of the two solutions. The normalised concentration, *c* *, is defined as:

$$c^* = \frac{c - c_{min}}{c_{max} - c_{min}} \tag{4}$$

where *c* is the concentration of the species in solution, and the subscripts indicate the minimum (*min*) and maximum (*max*) concentration values. Homogeneity, in terms of mixing, is characterised by the standard deviation (σ_{st}) of the sampling points along the concentration profile for a particular probe point [46], i.e.,

$$\sigma_{st} = \sqrt{\frac{1}{N} \sum_{i=1}^{N} \left(c_i^* - c_m^*\right)^2} \tag{5}$$

where N is the number of sampling points, c_i^* is the normalised concentration at point i, and c_m^* is the mean normalised concentration. The mixing efficiency (η_{mixing}) is thus defined as:

$$\eta_{mixing} = 1 - \sqrt{\frac{1}{N}\sum_{i=1}^{N}\left(\frac{c_i^* - c_m^*}{c_i^*}\right)^2} \qquad (6)$$

The mixing efficiency was measured at each of the 12 probe points (shown in Figure 3a shows the simulated velocity magnitude distribution within the serpentine micromixer. The serpentine geometry causes the maximum fluid velocity to vary, moving from the centre of the microchannel towards the edges along the x-direction [43]. This is a key characteristic required to induce chaotic flow in low Reynolds number microfluidic systems, where it is essential to have transverse components of liquid flow that stretch and fold volumes of fluid over the cross-section of the microfluidic channel. This is the mechanism via which the serpentine geometry induces stirring flows, which in turn leads to a decreased average distance over which the diffusion occurs. As the geometrical and liquid parameters are constant, the chaotic flow reaches a steady state, where the stretching and folding of volumes of the fluid proceed exponentially as a function of the axial distance travelled by the fluid volume. This is related to the characteristic length which depends on the geometry of the fabricated microfluidic system: $\Delta y = t \cdot exp(-\Delta x/l)$, where t is the initial transverse distance [44,45].

The Peclet number is a physical quantity defined as the ratio of the rate of the convective mass transport to the rate of diffusion mass transport. The Peclet number is given by $Pe = ul/D$, where l is the characteristic length (the distance over which the species must mix). In the present case where we have chaotic mixing occurring, the hydraulic diameter of the channel is defined as the characteristic length scale and is given by $4A/P_w$ where A is the cross-sectional area, and P_w is the wetted perimeter of the channel at the cross-section. For the present simulation, due to the low diffusivity of fluorescein in water and a relatively high-velocity range of 1.89–4.72 m/s, the maximum values of Pe are around 65,000. A large Pe indicates a convective dominated mass transport, which in this case is highly dependent on the chaotic advection phenomenon in the mixer microchannel [46]. The micro-mixer areas, where the chaotic advection effect is higher, are shown by the darker blue regions within the Peclet number distribution (Figure 3b). Figure 3b shows clear periodic perturbations, characteristic of the stretching and folding of fluid volumes, which are associated with chaotic advection. The darkest spots (highest Pe) in Figure 3b are in the centre of the U-bend shapes, indicating a constriction in the flow due to the resistance created by the microchannel walls because of the serpentine geometry. The value of Pe also peaks near the outlet because of the sudden release of the flow due to the lack of microchannel wall resistance near the outlet.) for the serpentine micro-mixer. The experimental mixing efficiencies were calculated using normalised fluorescent light intensities, which directly correlate to the normalised concentration values [46]. Figure 5 compares some examples of experimental and simulation results for two different flow rates. Below a mixer length of approximately 750 μm, we note that some of the associated errors on the experimental data are comparatively larger than at longer channel lengths. As discussed earlier, the simulations neglect any effects due to micro-fabrication errors. We hypothesize that the larger errors within this regime are due to the fact that minor defects in the fabrication may have a more significant effect when mixing over shorter distances. However, we do find that the overall trend of the experimental mixing efficiency as a function of distance along the serpentine mixer is reproduced in the FEM simulations.
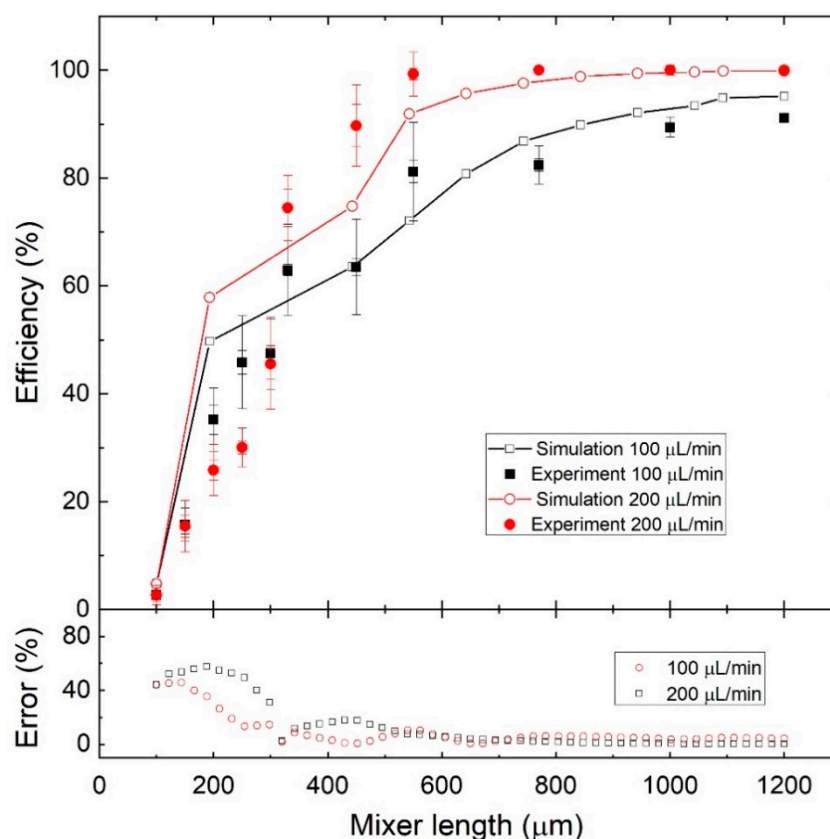
Figure 5. (**a**) Comparison of the simulated and experimental results of the mixing efficiency versus the mixing length along the serpentine mixing channel for two different flow rates: 100 and 200 µL/min; (**b**) the deviation (error) in % between simulated and experimental results.

At a flow rate of 100 µL/min, both the simulated and experimental results reach a peak mixing efficiency of around 95% at the outlet (mixer length = 1200 µm). For the higher flow rate of 200 µL/min, 95% mixing efficiency is already achieved at around 800 µm, indicating that at higher flow rates, a shorter serpentine length is required to achieve uniform mixing. Homogeneous mixing over shorter length scales is critical for solution scattering experiments where it is important that any changes in molecular conformation are triggered at the same time, such that the majority of target molecules are in approximately the same conformational state. The similarity of the simulated and experimental results provides us with confidence that the simulations can be used to predict the geometries and mixing times required to achieve homogeneous mixing of the reactants for a range of input parameters.

3.2. Effect of Flow Rate

Mixing efficiencies were calculated for the 12 probe points along the length of the serpentine micromixer and for the flow rates in the range of 80–200 µL/min (where stable jetting is observed). Figure 6 shows that based on the numerical results, there is a rapid increase in mixing efficiency for mixer lengths between $x = 100$ and $x = 600$ µm due to the high concentration gradient in the first half of the serpentine mixer. Within the second half of the serpentine mixer ($x > 600$ µm), the mixing efficiency continues to increase, albeit with a gentler slope, until uniform mixing is achieved at the outlet.
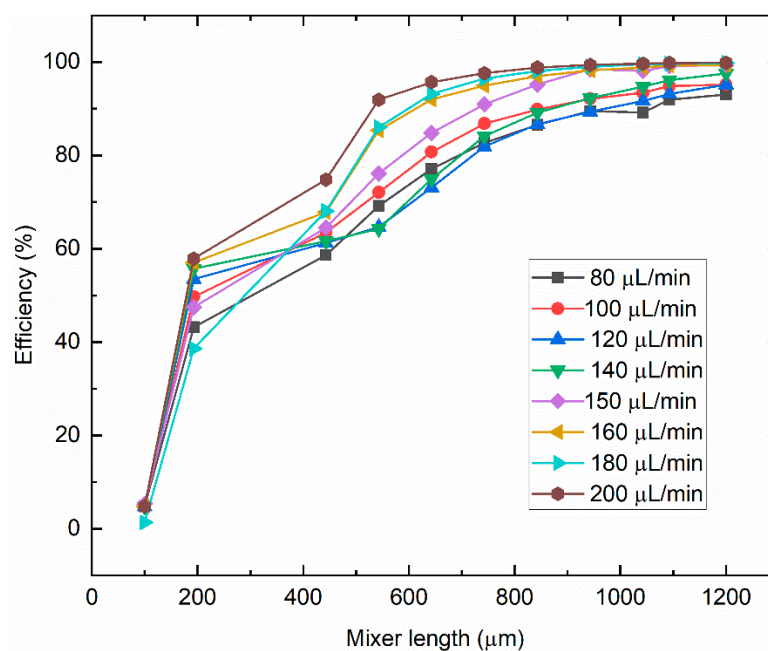
Figure 6. Numerical results: Mixing efficiency as a function of the serpentine mixer length for flow rates in the range of 80–200 μL/min. Within this flow rate range, our 1200 μm long serpentine micromixers can achieve homogenous (>90 %) mixing whilst producing a stable liquid jet for sample delivery at the outlet.

Even at the lowest flow rate of 80 μL/min, the serpentine micromixer reaches a maximum mixing efficiency of 93% at the outlet. Whilst for flow rates higher than 100 μL/min, the mixing efficiency at the liquid jet outlet is between 95–100%. An increase in the flow rate increases the average velocity magnitude in the mixer microchannel. The increase in the average velocity translates to the dominance of advective mass transport over the diffusive one. For example, for an increase from 100 μL/min to 180 μL/min, the average velocity increases from 2.39 to 4.25 m/s, which leads to an increase in the average value for Pe from 15,770 to 29,269. Hence, the mixing efficiency is improved at higher flow rates due to an enhanced chaotic advection effect caused by the serpentine geometry. We should note, however, that whilst the higher flow rates enable faster, more homogeneous mixing resulting in a more conformationally uniform mixture, this comes at the cost of higher sample consumption, which can be an important consideration when dealing with expensive or scarce protein solutions.

3.3. Effect of Microchannel Size

We next used our FEM simulation to explore the effect of the mixer micro-channel dimensions on the mixing efficiency. Figure 7 shows the mixing efficiencies as a function of the serpentine mixer length for three different height-to-width ratios (r = H/W): 0.9, 1.8, and 3.6 at a constant flow rate of 100 μL/min. Figure 7a shows the mixing efficiencies for H = 45 μm and W = 12.5, 25, and 50 μm, respectively. Figure 7b shows the mixing efficiencies for H = 22.5, 45, and 90 μm for W = 25 μm.

The results in Figure 7a indicate that for a fixed height of H = 45 μm and a channel width of W = 12.5 μm (r = 3.6), the micro-mixer can achieve mixing efficiencies of over 90%, faster than for W = 25 and 50 μm, and that to achieve the same mixing efficiency with a wider channel, a longer channel length is required. In addition, wider channels also require more of the sample to maintain the same flow rate and, hence, sample consumption can be an issue. However, whilst the narrower microchannels appear to be more efficient at mixing, these also have the disadvantage that when mixing and jetting biological samples, the channels can potentially become blocked. When examining the effect of height in Figure 7b for a fixed channel width of W = 25 μm, we find that the most efficient mixing

occurs for H = 22.5 μm (r = 0.9). The largest height (H = 90 μm) gives the least efficient mixing, whilst a channel height of (H = 45 μm) provides an intermediate mixing efficiency. The average Reynolds number for the devices that was used in the experimental studies (r = 1.8) is Re = 2.13, whilst Re = 4.27 for r = 3.6, and Re = 1.07 for r = 0.9. The results from Figure 7a,b indicate that a smaller microchannel cross-section results in uniform mixing that is faster and has higher efficiency due to an increase in the average velocity of the solutions and consequently has an enhanced chaotic mixing effect.
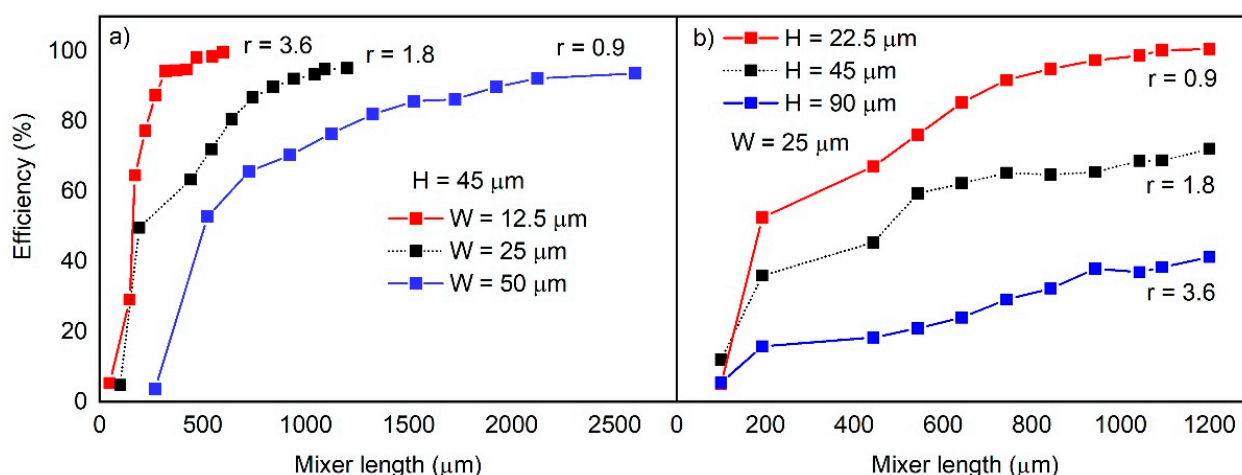
Figure 7. Mixing efficiencies along the length of the serpentine micromixer for (**a**) H = 45 μm, W = 12.5, 25 and 50 μm, and (**b**) W = 25 μm, H = 22.5, 45, and 90 μm at a flow rate of 100 μL/min. The aspect ratios are r = 0.9, 1.8, and 3.6. The simulated results matching the height-to-width ratio used experimentally (represented in (**a**) and (**b**) by a dotted line) has an aspect ratio of r = H/W = 1.8 and is included for comparison.

The fabrication approach using SU8 developed for our microfluidic devices enables highly flexible geometries to be achieved without requiring any alteration of the photolithography mask design. This means that all of the ratios in terms of height and width simulated here can be readily reproduced experimentally and, according to our previous experimental work [40,41], will also result in stable jetting. Ratios are r = 0.9, 1.8, and 3.6.

The minimum achievable mixing times for the serpentine micromixer as a function of the flow rate are shown in Figure 8; the smaller the serpentine, the faster the mixing. The minimum achievable mixing time is defined here as the amount of time required for the reagents to travel in the serpentine micromixer before at least 95% mixing efficiency is achieved. Consistent with the results in Figure 7, Figure 8a shows that for a fixed channel height (H = 45 μm), as the channel width increases, the minimum achievable mixing time also increases (from 0.30 ms for W = 12.5 μm to 1.28 ms for W = 50 μm) and that even increasing the flow rate to 300 μL/min cannot make up for the difference in mixing times compared to the 12.5 and 25 μm width channels. By decreasing the channel width to 12.5 μm, we can maintain sub-ms mixing (0.85 ms), even with flow rates as low as 120 μL/min whilst still maintaining a stable jet. Figure 8b shows that for a fixed channel width (W = 45 μm) as the height of the mixing channel decreases, shorter and shorter mixing times can be achieved for a given flow rate. With the thinnest mixer (H = 22.5 μm) sub-ms mixing times can be achieved with flow rates as low as 80 μL/min. In fact, by using a micromixer channel of dimensions 22.5 μm × 25 μm (H × W) it is possible to achieve mixing times in the range of 0.5–3.4 ms using flow rates of 40–100 μL/min. These parameters are readily achievable experimentally and indicate that our mix-and-inject devices could be employed to study a wide range of biomolecular dynamics [32] with minimal sample consumption.
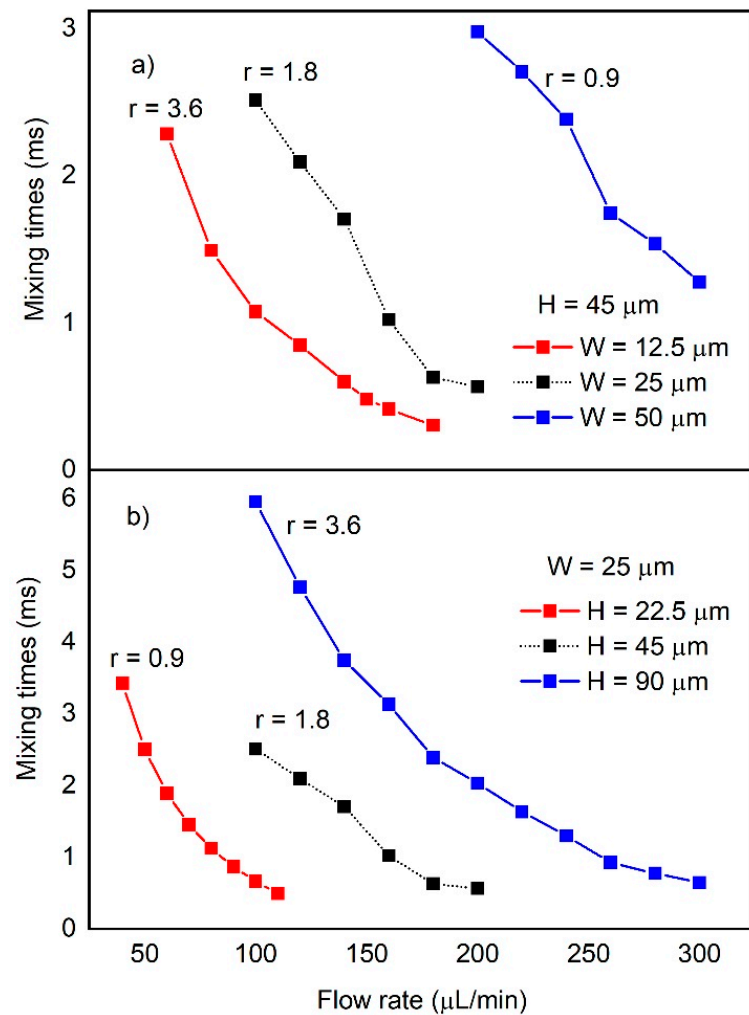
Figure 8. Minimum achievable mixing time (in milliseconds) using a serpentine micromixer for (**a**) H = 45 μm, W = 12.5, 25, and 50 μm, and (**b**) W = 25 μm, H = 22.5, 45, and 90 μm as a function of flow rate. The aspect results matching the height-to-width ratio used experimentally (represented in (**a**) and (**b**) by a dotted line) has an aspect ratio of r = H/W = 1.8 and is included for comparison.

4. Conclusions

Here, we have presented the results of the 3D FEM simulations modelling of chaotic advection in passive serpentine-micromixers. We have determined concentration profiles along the length of the serpentine micromixer at 12 different probe points. The results show that our serpentine micromixers can achieve uniform mixing using flow rates as low as 80 μL/min, which is consistent with our experimental data using these devices. The results also show that the chaotic mixing effect significantly increases at higher flow rates, resulting in faster mixing of the reagents. Moreover, we have used simulations to evaluate the impact of the microchannel dimensions on the mixing efficiency of the devices. The results indicate that for a channel width of W = 12.5 μm and height H = 45 μm, the serpentine micromixer can achieve uniform mixing within a shorter serpentine length, equating to a reduction in the minimum achievable mixing time required to reach >95% mixing efficiency. Further, we have calculated mixing times for a wide range of different flow rates and different cross-sectional aspect ratios of the serpentine micromixer channel. The results show that micromixers with a smaller cross-sectional area can achieve uniform mixing with lower flow rates and shorter mixing times. Both the simulated and experimental results indicate that the serpentine micromixer is an efficient and straightforward method for achieving sub-millisecond and millisecond mix-and-inject devices for studying molecular dynamics. The size of the microchannels can be optimised based on operational factors such as the

amount of sample solution available for the experiment, the timescales of the reaction kinetics being probed, the required velocity and diameter of the liquid jet (i.e., to match the size of the X-ray beam), and whether or not the sample is likely to contain particles larger than ~0.1 μm. The simulation results reported here will guide the future development of rapid mix-and-inject microfluidic devices, providing new insights into biomolecule structures and dynamics.

Nomenclature

A	Cross-sectional area (m^2)
c	Concentration (mol/m^3)
$c*$	Normalised concentration
c_i^*	Normalised concentration at point i
c_m^*	Mean normalised concentration
D	Diffusion coefficient of the solute (m^2/s)
F	Volume force vector (N/m^3)
H	Height of the mixer microchannel (m)
K	Viscous stress tensor (Pa)
I	Identity matrix
l	Characteristic length (m)
N	Number of sampling points
p	Pressure inside the mixer microchannel (Pa)
P_w	The wetted perimeter of the channel (m)
Pe	Peclet number
r	Height-to-width ratios (r = H/W)
u	Velocity vector (m/s)
W	Width of the mixer microchannel (m)
η_{miximg}	Mixing efficiency (m)
ρ	Solution density (kg/m^3)
σ_{st}	Standard deviation

References

1. Neutze, R.; Moffat, K. Time-resolved structural studies at synchrotrons and *x*-ray free electron lasers: Opportunities and challenges. *Curr. Opin. Struct. Biol.* **2012**, *22*, 651–659. [CrossRef]
2. Schulz, J.; Bielecki, J.; Doak, R.B.; Dörner, K.; Graceffa, R.; Shoeman, R.L.; Sikorski, M.; Thute, P.; Westphal, D.; Mancuso, A.P. A versatile liquid-jet setup for the European XFEL. *J. Synchrotron Radiat.* **2019**, *26*, 339–345. [CrossRef]
3. Grunbein, M.L.; Kovacs, G.N. Sample delivery for serial crystallography at free-electron lasers and synchrotrons. *Acta Crystallogr. Sect. D* **2019**, *75*, 178–191. [CrossRef] [PubMed]

4.   Martiel, I.; Muller-Werkmeister, H.M.; Cohen, A.E. Strategies for sample delivery for femtosecond crystallography. *Acta Crystallogr. Section D* **2019**, *75*, 160–177. [CrossRef]

5.   Zhao, F.-Z.; Zhang, B.; Yan, E.K.; Sun, B.; Wang, Z.J.; He, J.H.; Yin, D.C. A guide to sample delivery systems for serial crystallography. *FEBS J.* **2019**, *286*, 4402–4417. [CrossRef] [PubMed]

6.   Steinke, I.; Walther, M.; Lehmkühler, F.; Wochner, P.; Valerio, J.; Mager, R.; Schroer, M.A.; Lee, S.; Roseker, W.; Jain, A.; et al. A liquid jet setup for *x*-ray scattering experiments on complex liquids at free-electron laser sources. *Rev. Sci. Instrum.* **2016**, *87*, 063905. [CrossRef]

7.   Ward, K.; Fan, Z.H. Mixing in microfluidic devices and enhancement methods. *J. Micromech. Microeng.* **2015**, *25*, 094001. [CrossRef] [PubMed]

8.   Lee, C.-Y.; Chang, C.L.; Wang, Y.N.; Fu, L.M. Microfluidic mixing: A review. *Int. J. Mol. Sci.* **2011**, *12*, 3263–3287. [CrossRef] [PubMed]

9.   Lee, C.-Y.; Wang, W.T.; Liu, C.C.; Fu, L.M. Passive mixers in microfluidic systems: A review. *Chem. Eng. J.* **2016**, *288*, 146–160. [CrossRef]

10.   Chen, X.; Shen, J. Simulation and experimental analysis of a SAR micromixer with F-shape mixing units. *Anal. Methods* **2017**, *9*, 1885–1890. [CrossRef]

11.   Zare, P.; Talebi, S. Numerical simulation of geometry effect on mixing performance in L-shaped micromixers. *Chem. Eng. Commun.* **2020**, *207*, 585–597. [CrossRef]

12.   Chen, X.; Shen, J. Numerical and experimental investigation on splitting-and-recombination micromixer with E-shape mixing units. *Microsyst. Technol.* **2017**, *23*, 4671–4677. [CrossRef]

13.   Chung, C.K.; Chang, C.K.; Lai, C.C. Simulation and fabrication of a branch-channel rhombic micromixer for low pressure drop and short mixing length. *Microsyst. Technol.* **2014**, *20*, 1981–1986. [CrossRef]

14.   Wu, C.; Tang, K.; Gu, B.; Deng, J.; Liu, Z.; Wu, Z. Concentration-dependent viscous mixing in microfluidics: Modelings and experiments. *Microfluid. Nanofluidics* **2016**, *20*, 90. [CrossRef]

15.   Bazaz, S.R.; Amiri, H.A.; Vasilescu, S.; Mehrizi, A.A.; Jin, D.; Miansari, M.; Warkiani, M.E. Obstacle-free planar hybrid micromixer with low pressure drop. *Microfluid. Nanofluidics* **2020**, *24*, 61. [CrossRef]

16.   Tsai, R.-T.; Wu, C.-Y. An efficient micromixer based on multidirectional vortices due to baffles and channel curvature. *Biomicrofluidics* **2011**, *5*, 014103. [CrossRef]

17.   Melin, J.; Giménez, G.; Roxhed, N.; Van der Wijngaart, W.; Stemme, G. A fast passive and planar liquid sample micromixer. *Lab Chip* **2004**, *4*, 214–219. [CrossRef]

18.   Chen, X.; Zhang, S. 3D micromixers based on Koch fractal principle. *Microsyst. Technol.* **2018**, *24*, 2627–2636. [CrossRef]

19.   Shi, X.; Huang, S.; Wang, L.; Li, F. Numerical analysis of passive micromixer with novel obstacle design. *J. Dispers. Sci. Technol.* **2019**, *42*, 440–456. [CrossRef]

20.   Wu, S.-J.; Hsu, H.-C.; Feng, W.-J. Novel design and fabrication of a geometrical obstacle-embedded micromixer with notched wall. *Jpn. J. Appl. Phys.* **2014**, *53*, 097201. [CrossRef]

21.   Bernacka-Wojcik, I.; Ribeiro, S.; Wojcik, P.J.; Alves, P.U.; Busani, T.; Fortunato, E.; Baptista, P.V.; Covas, J.A.; Águas, H.; Hilliou, L.; et al. Experimental optimization of a passive planar rhombic micromixer with obstacles for effective mixing in a short channel length. *RSC Adv.* **2014**, *4*, 56013–56025. [CrossRef]

22.   Shi, X.; Wang, L.; Huang, S.; Li, F. A novel passive micromixer with array of Koch fractal obstacles in microchannel. *J. Dispers. Sci. Technol.* **2019**, *42*, 236–247. [CrossRef]

23.   Chen, X.; Zhao, Z. Numerical investigation on layout optimization of obstacles in a three-dimensional passive micromixer. *Anal. Chim. Acta* **2017**, *964*, 142–149. [CrossRef] [PubMed]

24.   Solehati, N.; Bae, J.; Sasmito, A.P. Numerical investigation of mixing performance in microchannel T-junction with wavy structure. *Comput. Fluids* **2014**, *96*, 10–19. [CrossRef]

25.   Chen, X.; Li, T. A novel passive micromixer designed by applying an optimization algorithm to the zigzag microchannel. *Chem. Eng. J.* **2017**, *313*, 1406–1414. [CrossRef]

26.   COMSOL Multiphysics®v. 5.6. COMSOL AB, Stockholm, Sweden. Available online: www.comsol.com (accessed on 9 April 2021).

27.   Liu, C.; Li, Y.; Liu, B.-F. Micromixers and their applications in kinetic analysis of biochemical reactions. *Talanta* **2019**, *205*, 120136. [CrossRef] [PubMed]

28.   Jiang, L.; Zeng, Y.; Zhou, H.; Qu, J.Y.; Yao, S. Visualizing millisecond chaotic mixing dynamics in microdroplets: A direct comparison of experiment and simulation. *Biomicrofluidics* **2012**, *6*, 012810. [CrossRef]

29.   Song, H.; Ismagilov, R.F. Millisecond kinetics on a microfluidic chip using nanoliters of reagents. *J. Am. Chem. Soc.* **2003**, *125*, 14613–14619. [CrossRef]

30.   Chen, C.; Zhao, S.; Zhu, P.; Shi, J.; Yan, F.; Xia, H.; Shen, R. Improvement of silver azide crystal morphology and detonation behavior by fast mixing using a microreaction system with an integrated static micromixer. *React. Chem. Eng.* **2020**, *5*, 154–162. [CrossRef]

31.   Pal, S. Chapter 7—Protein Folding. In *Fundamentals of Molecular Structural Biology*; Pal, S., Ed.; Academic Press: Cambridge, MA, USA, 2020; pp. 149–169.

32.   Lindorff-Larsen, K.; Maragakis, P.; Piana, S.; Shaw, D.E. Picosecond to millisecond structural dynamics in human ubiquitin. *J. Phys. Chem. B* **2016**, *120*, 8313–8320. [CrossRef]

33. Sekhar, A.; Vallurupalli, P.; Kay, L.E. Defining a length scale for millisecond-timescale protein conformational exchange. *Proc. Natl. Acad. Sci. USA* **2013**, *110*, 11391–11396. [CrossRef] [PubMed]

34. Strack, R. XFELs probe protein dynamics. *Nat. Methods* **2015**, *12*, 109. [CrossRef] [PubMed]

35. Kang, Y.; Zhou, X.E.; Gao, X.; He, Y.; Liu, W.; Ishchenko, A.; Barty, A.; White, T.A.; Yefanov, O.; Han, G.W.; et al. Crystal structure of rhodopsin bound to arrestin by femtosecond *x*-ray laser. *Nature* **2015**, *523*, 561–567. [CrossRef]

36. Knoška, J.; Adriano, L.; Awel, S.; Beyerlein, K.R.; Yefanov, O.; Oberthuer, D.; Murillo, G.E.P.; Roth, N.; Sarrou, I.; Villanueva-Perez, P.; et al. Ultracompact 3D microfluidics for time-resolved structural biology. *Nat. Commun.* **2020**, *11*, 657. [CrossRef]

37. Kim, H.; Min, K.I.; Inoue, K.; Kim, D.P.; Yoshida, J.I. Submillisecond organic synthesis: Outpacing Fries rearrangement through microfluidic rapid mixing. *Science* **2016**, *352*, 691. [CrossRef] [PubMed]

38. Mäeots, M.-E.; Lee, B.; Nans, A.; Jeong, S.G.; Esfahani, M.M.; Ding, S.; Smith, D.J.; Lee, C.S.; Lee, S.S.; Peter, M.; et al. Modular microfluidics enables kinetic insight from time-resolved cryo-EM. *Nat. Commun.* **2020**, *11*, 3465. [CrossRef]

39. Jones, S.W.; Thomas, O.M.; Aref, H. Chaotic advection by laminar flow in a twisted pipe. *J. Fluid Mech.* **1989**, *209*, 335–357. [CrossRef]

40. Hejazian, M.; Darmanin, C.; Balaur, E.; Abbey, B. Mixing and jetting analysis using continuous flow microfluidic sample delivery devices. *RSC Adv.* **2020**, *10*, 15694–15701. [CrossRef]

41. Hejazian, M.; Balaur, E.; Flueckiger, L.; Hor, L.; Darmanin, C.; Abbey, B. Microfluidic mixing and jetting devices based on SU8 and glass for time-resolved molecular imaging experiments. *Proc. SPIE* **2019**, *10875*, 108750D.

42. Rani, S.A.; Pitts, B.; Stewart, P.S. Rapid diffusion of fluorescent tracers into Staphylococcus epidermidis biofilms visualized by time lapse microscopy. *Antimicrob. Agents Chemother.* **2005**, *49*, 728–732. [CrossRef]

43. Zhang, H.; Li, X.; Chuai, R.; Zhang, Y. Chaotic Micromixer Based on 3D Horseshoe Transformation. *Micromachines* **2019**, *10*, 398. [CrossRef] [PubMed]

44. Rosensweig, R.E. *The Kinematics of Mixing: Stretching, Chaos, and Transport*; Ottino, J.M., Ed.; Cambridge Texts in Applied Mathematics; Cambridge University Press: Cambridge, UK, 1989.

45. Simonnet, C.; Groisman, A. Chaotic mixing in a steady flow in a microchannel. *Phys. Rev. Lett.* **2005**, *94*, 134501. [CrossRef] [PubMed]

46. Nguyen, N.T. *Micro and Nano Technologies, Micromixers*, 2nd ed.; Elsevier/William Andrew: Amsterdam, The Netherlands, 2012.